

# Photoelectrical detection of nitrogen-vacancy centers by utilizing diamond lateral p-i-n diodes

Cite as: Appl. Phys. Lett. **118**, 253502 (2021); doi: [10.1063/5.0055852](https://doi.org/10.1063/5.0055852)

Submitted: 4 May 2021 · Accepted: 27 May 2021 ·

Published Online: 25 June 2021



View Online



Export Citation



CrossMark

T. Murooka,<sup>1</sup> M. Shiigai,<sup>1</sup> Y. Hironaka,<sup>1</sup> T. Tsuji,<sup>1</sup> B. Yang,<sup>1</sup> T. M. Hoang,<sup>1</sup> K. Suda,<sup>1</sup> K. Mizuno,<sup>1</sup> H. Kato,<sup>2</sup> T. Makino,<sup>2</sup> M. Ogura,<sup>2</sup> S. Yamasaki,<sup>2</sup> M. Hatano,<sup>1</sup> and T. Iwasaki<sup>1,a)</sup>

## AFFILIATIONS

<sup>1</sup>School of Engineering, Department of Electrical and Electronic Engineering, Tokyo Institute of Technology, Ookayama, Meguro, Tokyo 152-8552, Japan

<sup>2</sup>Advanced Power Electronics Research Center, National Institute of Advanced Industrial Science and Technology, Umezono, Tsukuba, Ibaraki 305-8568, Japan

<sup>a)</sup> Author to whom correspondence should be addressed: [iwasaki.taj@m.titech.ac.jp](mailto:iwasaki.taj@m.titech.ac.jp)

## ABSTRACT

We demonstrate a photoelectrical readout of negatively charged nitrogen-vacancy ( $\text{NV}^-$ ) centers by utilizing a lateral diamond p-i-n diode structure. We found that the photocarriers generated at NV centers are efficiently extracted in the depletion layer even at zero voltage. The transport mechanism for photoexcited minority carriers was investigated by varying the nitrogen ion implantation dose. The minority carrier diffusion length decreased when the photocarriers passed through the implantation region, particularly at a high nitrogen ion dose. From photoelectrically detected magnetic resonance (PDMR) measurements, the photocurrent was found to exhibit a minimum at approximately 2.87 GHz upon microwave irradiation with a contrast of 12%, while this dip was observed to split upon the application of a static magnetic field. The PDMR signal was found to depend on the measurement position. This study paves the way for efficient electrical detection for quantum sensors based on device technologies.

Published under an exclusive license by AIP Publishing. <https://doi.org/10.1063/5.0055852>

The negatively charged nitrogen vacancy ( $\text{NV}^-$ ) center in diamond is a promising system for solid-state quantum devices such as quantum sensors and single-photon sources.<sup>1–3</sup> Although optical detection is typically utilized to readout the spin state of a  $\text{NV}^-$ , the photon collection efficiency is limited by the high refractive index of diamond of 2.4.<sup>4</sup> The total detection efficiency is further degraded considering losses at optical components and the detection efficiency of the photodetector, limiting the sensitivity of the sensor. Moreover, it is disadvantageous from the viewpoint of system integration owing to the requirement of external photodetectors and optics. The photoelectrical readout technique is another approach for detecting NV centers, in which the spin states are readout as a spin-dependent photocurrent instead of fluorescence. The photoelectrical readout of  $\text{NV}^-$  electron spins was recently demonstrated for the first time by Bourgeois *et al.*<sup>5</sup> Hrubesch *et al.* theoretically predicted that the spin detection sensitivity of the photoelectrical method is more than three times that of the optical method using pulsed spin manipulation and readout schemes.<sup>6</sup> Siyushev *et al.* reported high signal-to-noise-ratio (SNR) measurements for a single NV center compared to optical detection.<sup>7</sup> Moreover, <sup>14</sup>N nuclear spin coherence for an ensemble of NV centers

was detected by Morishita *et al.*,<sup>8</sup> and, recently, single nuclear spin detection was also reported by Gulka *et al.*<sup>9</sup> In addition to the advantages of system integration, the photoelectrical detection technique is expected to provide nanoscale detection exceeding the diffraction limit without super-resolution fluorescence microscopy by creating NV centers in a nanoscale device.<sup>10</sup> These characteristics indicate a high potential for the photoelectrical detection of NV centers. Thus, the establishment of the photoelectrical readout technique will have an essential role in the development of diamond-based quantum sensors.

In photocurrent detection, the photocarriers generated from the NV centers are transported to and then collected by the electrodes. Thus, understanding the photocarrier transport mechanism is crucial to apply photoelectrical detection techniques for highly sensitive magnetometers. However, the transport mechanism for the photocarriers generated upon laser illumination of the NV centers has yet to be revealed. In this study, we investigated the diffusion length of minority carriers using a diamond lateral p-i-n diode structure incorporating an ensemble of NV centers. The detection of the photocurrent as a function of the laser position in the i-layer enables us to estimate the diffusion length of the minority carriers. In addition to the estimation

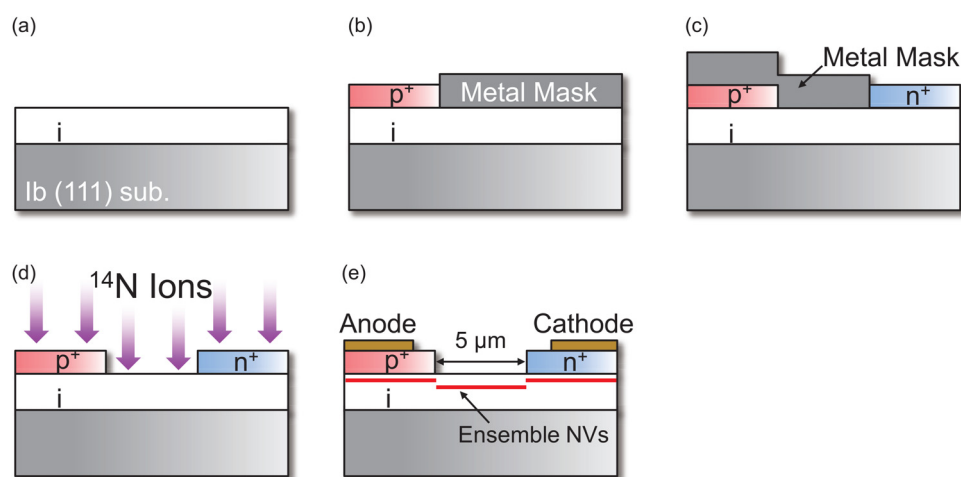
of the diffusion length, the p-i-n diode is a structure that would lead to carrier multiplication in avalanche mode operation. As the basis, we investigated the detection of the photocurrent and photoelectrically detected magnetic resonance (PDMR) of the NV centers in p-i-n diodes with varying applied biases up to 10 V. We found that photoexcited carriers from the NV centers were efficiently collected even at zero voltage because of the high built-in potential of  $\sim 4.5$  V in the diamond p-n junction. Photoelectrical detection has been previously performed in metal-insulator-metal or metal-semiconductor-metal structures,<sup>5–8,11,12</sup> while in this study, we demonstrate photoelectrical detection using a diamond p-i-n diode structure.

Figure 1 illustrates the fabrication of the diamond lateral p-i-n diodes. A 5  $\mu\text{m}$ -thick intrinsic diamond layer was grown onto a (111) Ib-type single-crystal diamond substrate by microwave-plasma-enhanced chemical vapor deposition (MPCVD) [Fig. 1(a)]. This i-layer was lightly doped with phosphorus ( $[P] \sim 10^{16} \text{ cm}^{-3}$ ) to stabilize the negative charge state of the NV center.<sup>13</sup> Following i-layer growth, patterned boron-doped p<sup>+</sup>-type ( $[B] \sim 10^{20} \text{ cm}^{-3}$ ) and phosphorus-doped n<sup>+</sup>-type ( $[P] \sim 10^{20} \text{ cm}^{-3}$ ) diamond regions were individually grown on the top of the i-layer by MPCVD with metal masks patterned by photolithography and deposited by electron-beam evaporation [Figs. 1(b) and 1(c)].<sup>14</sup> The spacing between the p<sup>+</sup>- and n<sup>+</sup>-layers was designed to be 5  $\mu\text{m}$ . Ensemble NV centers were formed in the p-i-n diode using ion implantation [Fig. 1(d)]. We prepared devices on two diamond substrates with different nitrogen dose configurations. For the first sample (sample #h879), <sup>14</sup>N ions were implanted over the whole surface at a dose of  $10^{12} \text{ cm}^{-2}$ . For the second sample (sample #h877), devices with different ion doses ( $10^{11}$ ,  $10^{12}$ , and  $10^{13} \text{ cm}^{-2}$ ) were fabricated on the same substrate to perform identical processes. The second sample was used to investigate the dose dependence of the minority carrier diffusion length (Fig. 4) and position-dependent PDMR [Fig. 5(c)]. All other measurements were carried out using the first sample. The acceleration energy was 350 keV, leading to a projected depth of 350 nm. Ion implantation was performed at 600 °C to suppress implantation damage. The specimen was then annealed at 1000 °C in vacuum for 1 h. NV centers were also formed

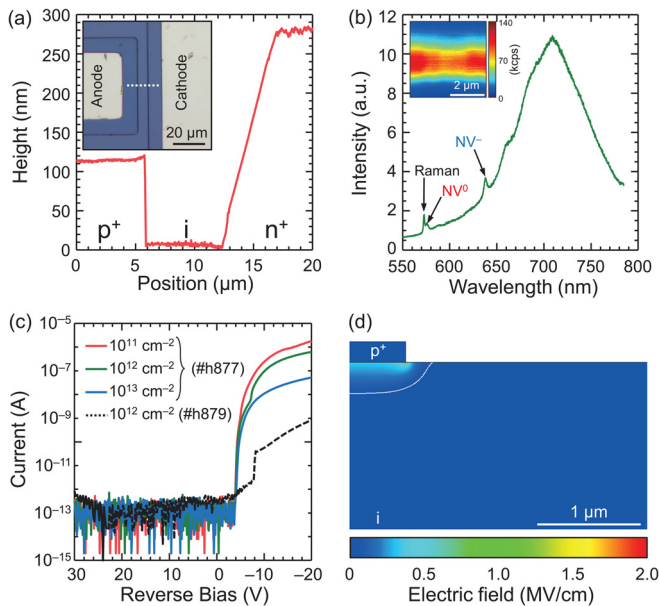
under the p<sup>+</sup>- and n<sup>+</sup>-layers. After NV center formation, the specimen was treated with an acid mixture ( $\text{H}_2\text{SO}_4$  and  $\text{HNO}_3$ ) to terminate the diamond surface with oxygen. Finally, Ti (30 nm)/Pt (30 nm)/Au (100 nm) stacks were deposited by electron-beam evaporation and subsequently annealed at 420 °C in air for 30 min to achieve good contact properties [Fig. 1(e)].<sup>15</sup>

Figure 2(a) shows the height profile of the fabricated p-i-n diode observed by atomic force microscopy, confirming the growth of the p<sup>+</sup>- and n<sup>+</sup>-regions on the i-layer. The thicknesses of the p<sup>+</sup>- and n<sup>+</sup>-layers were approximately 110 and 280 nm, respectively. Hence, the peak depths for the nitrogen concentration under the p<sup>+</sup>- and n<sup>+</sup>-layers from the interface at the i-layer were expected to be 240 and 70 nm, respectively. The nitrogen distribution was calculated using the Stopping and Range of Ions in Matter (SRIM) software. (The simulated nitrogen profile is denoted in the [supplementary material](#)).<sup>16</sup>

A confocal fluorescence microscope image and photoluminescence (PL) spectrum were acquired to confirm NV center formation [Fig. 2(b)]. The NV centers were excited by illumination with a 532 nm laser through a 50 $\times$  air objective with a numerical aperture of 0.95. The fluorescence was detected with a single-photon counter through a neutral-density filter (NDF) with an optical density of 2. A continuous bright region was observed in the fluorescence map in the depth direction. The PL spectrum contained peaks originating from both negative and neutral charge states of the NV centers, as shown in Fig. 2(b). The fraction of the area of the zero-phonon line (ZPL) peak for NV<sup>-</sup> at the center of the exposed i-layer was  $\sim 57\%$  against the total ZPL area (both NV<sup>-</sup> and NV<sup>0</sup>), where a value of  $\sim 35\%$  was obtained from the NV centers formed in the type-IIa diamond substrate with a nitrogen ion dose of  $10^{12} \text{ cm}^{-2}$ . Thus, the negative charge state of the NV centers was stabilized in the lightly P-doped layer.<sup>17,18</sup> This fraction decreased to 40% in the device upon the application of a forward bias owing to the current injection,<sup>14,19</sup> while it gradually increased to  $\sim 70\%$  at 10 V for the reverse bias. The yield for the NV centers against the implanted nitrogen atoms was roughly estimated to be  $\sim 20\%$ , compared with the fluorescence from a single NV center, comparable to that of ensemble NV centers in a P-doped sample.<sup>17</sup>



**FIG. 1.** Fabrication of a lateral diamond p-i-n diode incorporating ensemble NV centers. (a) i-layer growth, (b) selective growth of the p<sup>+</sup>-layer, (c) selective growth of the n<sup>+</sup>-layer, (d) nitrogen ion implantation and subsequent annealing to form the NV center, and (e) electrode formation.



**FIG. 2.** Device characterization and simulation. (a) Height profile of the fabricated p-i-n diode measured along the dashed line in the optical microscopy image shown in the inset. (b) PL spectrum measured at a laser power of 5 mW. The inset is a cross-sectional confocal fluorescence microscope image of the i-layer observed at a laser power of 0.1 mW. Although the confocal image was obtained through use of an NDF with an optical density of 2, the fluorescence intensity of the present image was not corrected for the optical density. Note that an NDF was not used for the estimation of the yield. (c)  $I$ - $V$  curves for p-i-n diodes with implantation doses of  $10^{11}$ ,  $10^{12}$ , and  $10^{13}$  cm<sup>-2</sup>. The dashed curve represents the characteristics of a device with an implantation dose of  $10^{12}$  cm<sup>-2</sup> (sample #h879). (d) Device simulation at 0 V, showing the electric field distribution. The white curve represents the depletion layer edge.

The spin coherence time ( $T_2$ ) was measured to be approximately 10 μs at three positions, namely, under the p<sup>+</sup>-layer, at the exposed i-layer, and under the n<sup>+</sup>-layer, which is comparable to the reported value.<sup>20</sup>

Current-voltage ( $I$ - $V$ ) measurements of the fabricated p-i-n diodes incorporating the ensemble NV centers created by the different implantation doses were conducted with a semiconductor device analyzer (Agilent B1500A). The devices exhibited diode properties, as shown in Fig. 2(c), while the forward current decreased with increasing implantation dose. This reduction is caused by defects introduced by the implantation process. The dashed line shows the characteristics of the device with an implantation dose of  $10^{12}$  cm<sup>-2</sup> (sample #h879). The forward characteristics of this device differ from those of other three devices, despite the use of the same device fabrication process including NV center formation. Considering that the other devices showed typical diode properties, this is considered to be a device-specific characteristic. Note that since we mainly operated the devices at 0 V and for the reverse voltage conditions in this study, the forward characteristic does not affect the measurements. A device simulation (Sentaurus TCAD software) was carried out to estimate the depletion layer inside the device [Fig. 2(d)]. Details for the electric field simulation are presented in the [supplementary material](#). At 0 V, the depletion layer expanded from the p<sup>+</sup>-edge by approximately 0.30 and 0.23 μm in the depth and lateral directions, respectively. The magnitude of the electric field at the depletion edge under the p<sup>+</sup>-layer is ~32 kV/cm.

At the p<sup>+</sup>-edge, the electric field strength reaches ~2 MV/cm due to the local electric field concentration.

In this study, we measured the photocurrent by changing the voltage applied to the device. The operation mode at 0 V is referred to as photovoltaic, while that at a finite voltage is referred to as photoconductive. We measured the photocurrent from the NV centers in the i-layer under the p<sup>+</sup>-region in the photovoltaic mode [Fig. 3(a)]. The photocurrent was recorded with a transimpedance amplifier (NF Corporation CA5350) under different laser powers. The detected photocurrent increased as a quadratic function of the laser power up to 100 μW. The detection of the photocurrents in the photovoltaic mode implies that the photocarriers excited from NV<sup>-</sup> were efficiently collected by the electric field generated in the i-layer. The mechanism for the photoelectrical detection of NV<sup>-</sup> can be explained by a two-photon ionization process,<sup>5</sup> as illustrated in Fig. 3(b). First, an electron at the <sup>3</sup>A<sub>2</sub> triplet ground state of NV<sup>-</sup> is excited to the <sup>3</sup>E triplet excited state by the first photon. Second, the electron is photoionized to the conduction band by absorbing the second photon, leading to the charge state conversion of the NV centers from negative to neutral, i.e., NV<sup>-</sup> to NV<sup>0</sup>. In the third process, an electron is excited from <sup>2</sup>E to <sup>2</sup>A<sub>1</sub> for NV<sup>0</sup>, and finally, an electron is excited from the valence band to the vacant state of NV<sup>0</sup>, leading to the back conversion of the charge state to a negative state, as shown in Ref. 6. The free electrons and holes generated by the photoionization process generate the photocurrent. The cycle of this process enabled continuous detection of the photocurrent. Notably, the increasing tendency of the photocurrent became linear under higher illumination rather than quadratic, as

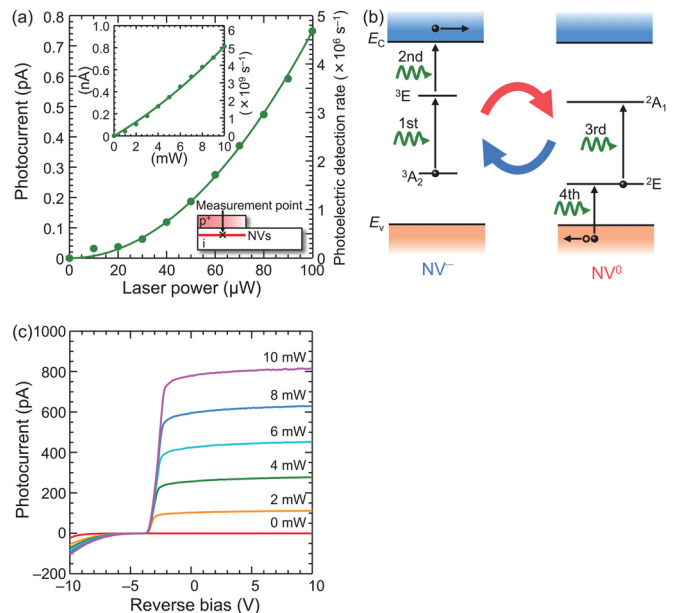


**FIG. 3.** Photocurrent measurements performed by using sample #h879. (a) Laser power dependence of the photocurrent in the photovoltaic operation mode (0 V). The solid line is a fitting curve obtained using Eq. (1). The fitting parameters are  $a = 7.47 \times 10^{-5}$  pA/μW<sup>2</sup> and  $b = 4.36 \times 10^{-6}$  pA/μW. The inset shows the photocurrent measured under higher illumination conditions. (b) Illustration of the principle of photocarrier generation. (c) Measured photocurrent as a function of the applied voltage at various laser powers.

depicted in the inset of Fig. 3(a). There are two possible factors for this phenomenon: saturation of the transition from  $^3A_2$  to  $^3E$ <sup>6,7</sup> and background signals originating from other defects, such as isolated substitutional nitrogen atoms, referred to as P1 centers.<sup>5</sup> Since the yield of the NV centers was estimated to be of the order of 20% in the present device, the rest of the implanted nitrogen can be converted to other defects. The measured photocurrent as a function of the laser power was fitted with

$$I_{\text{Photo}}(P) = aP^2 + bP, \quad (1)$$

where  $a$ ,  $b$ , and  $P$  are constants and the laser power, respectively.<sup>5</sup> As shown in Fig. 3(a), the experimental photocurrents were well fitted with this model. At 8 mW, the photocurrent and photoelectric detection rates were 624 pA and  $3.90 \times 10^9 \text{ s}^{-1}$ , corresponding to 1.60 pA and  $1 \times 10^7 \text{ s}^{-1}$  per single NV, respectively, taking into account the number of NV centers contributing to the photocurrent of  $\sim 390$ . The obtained photoelectric detection rate is comparable to the highest values reported for a metal-insulator-metal structure.<sup>7,12</sup> The photocurrent was also measured in the photoconductive mode up to 10 V for varying illumination power [Fig. 3(c)]. The voltage sweep and current recording were conducted with a power device analyzer (Keysight B1505A). The positive and negative biases represent the reverse and forward operations, respectively. The photocurrent rapidly increased at  $-3.2 \text{ V}$ , corresponding to an open-circuit voltage ( $V_{\text{OC}}$ ). After the steep increase in the photocurrent beyond  $V_{\text{OC}}$ , the photocurrent almost saturated. These device characteristics are the same as those found for photovoltaic devices such as solar cells and photodiodes. In Fig. 3(c), the negative currents flow at the forward negative voltages. These currents originate from the diode forward current and photocurrent, for which the holes now move in the opposite direction, i.e., from the  $p^+$ - to  $n^+$ -region. The low magnitude of the negative current is thought to be caused by the recombination of photocarriers and a large threshold voltage of this device [Fig. 2(c)].

We then investigated the minority carrier diffusion length generated upon laser illumination. Three devices with implantation doses of  $10^{11}$ ,  $10^{12}$ , and  $10^{13} \text{ cm}^{-2}$  were measured. The measurements were performed by detecting the photocurrent at 0 V, i.e., short-circuit current ( $I_{\text{SC}}$ ), while changing the position of the laser spot in the i-layer. Figure 4(a) shows the  $I_{\text{SC}}$  as a function of the measurement position. A region with almost constant photocurrent corresponds to the NV centers under the  $p^+$ -region. In contrast, the photocurrent exponentially decreased away from the  $p^+$ -edge in all three samples. The relationship between  $I_{\text{SC}}$  and the measurement position is given by<sup>21</sup>

$$I_{\text{SC}}(d) = I_0 \exp\left(-\frac{d}{L_d}\right), \quad (2)$$

where  $d$  and  $I_0$  are the distances in the analyzed range and current at  $d = 0$ , respectively, while  $L_d$  is the diffusion length of the minority carrier, which can be estimated by fitting the experimental photocurrent with this equation. The photocarriers generated in the depletion layer, i.e., close to the  $p^+$ -layer, were efficiently collected by the electrode, while, outside the depletion layer, the photocarriers suffered from recombination/trapping by defects in the crystal before reaching the depletion layer, decreasing the photocurrent, as observed. It is worth noting that the electric field distribution in the i-layer at 0 V strongly depends on the position (see the supplementary material). Thus, the

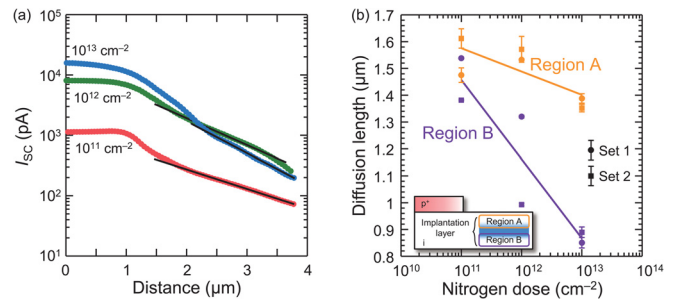


**FIG. 4.** Estimation of the minority carrier diffusion length. The measurements were performed by using sample #h877. (a) Photocurrent at 0 V as a function of the laser position at a constant laser power of 100 mW. The data were measured in region B mentioned in panel (b) for three devices with different nitrogen ion doses. The solid black lines represent fits to Eq. (2). The  $p^+$ -edges are located at a distance of approximately  $1 \mu\text{m}$ . (b) Diffusion lengths for the minority carriers at two positions, regions A and B, corresponding to the upper and lower areas of the implanted nitrogen distribution, respectively. We performed two sets of measurements for each region at two different locations, represented by the circle and square. The solid lines represent least-square fits to the data.

photocarriers might be transported not only by diffusion but also by drift with low electric fields, especially near the surface. Nevertheless, the photocarriers generated outside the depletion layer are not efficiently extracted, leading to the observed large reduction in photocarriers due to recombination/trapping by defects in the crystal. Thus, here, we call  $L_d$  the diffusion length. Figure 4(b) shows the estimated minority carrier diffusion lengths. To investigate the effect of the defects formed in the implanted region, we performed measurements at two different depths for laser focusing against the implanted nitrogen distribution. As observed in Fig. 2(b), owing to the limitation of the confocal setup (the spatial resolution in the depth direction of approximately  $1.6 \mu\text{m}$ ), the optical observation shows a wide distribution compared to the actual nitrogen distribution, which decreases by a factor of 10 at a depth of 50–100 nm away from the peak position confirmed by SRIM simulation (see the supplementary material). The laser spot was focused on the upper and lower positions  $2 \mu\text{m}$  apart in the fluorescence map in the depth direction. Thus, the laser is expected to dominantly measure the photocurrents from the NV centers at the corresponding positions, denoted as regions A and B, respectively. We performed two sets of experiments for each region at different positions. In region A, the diffusion length was estimated to be  $1.3\text{--}1.6 \mu\text{m}$ , slightly decreasing with increasing nitrogen ion dose. Such a decrease in diffusion length was also observed in region B, but the diffusion length largely decreased at doses of  $10^{12}$  and  $10^{13} \text{ cm}^{-2}$  down to  $\sim 0.85 \mu\text{m}$ . Note that the large deviation between the two sets for a dose of  $10^{12} \text{ cm}^{-2}$  could be caused by a slight difference in the measured depth. One reason for the lower values in region B should originate from the path of the photocarriers before reaching the depletion layer. The photocarriers from region A do not necessarily pass through the highly damaged implanted regions. In contrast, those photocarriers generated in region B inevitably pass through the region of the implantation peak before being collected at the electrodes, leading to carrier recombination, and, thus, to a reduction in the diffusion length. Indeed, the trends for a decrease in the diffusion length against the implantation dose are consistent with the degradation of the forward properties shown in Fig. 2(c). Notably, the minority carrier diffusion



lengths obtained in this study are larger than the value of  $0.43 \mu\text{m}$  estimated for a diamond bipolar junction field transistor with a higher phosphorus concentration of  $1 \times 10^{18} \text{ cm}^{-3}$ .<sup>22</sup> Although the proposed model here is very simplified, actual carrier transport should be more complex, e.g., a small fraction of the photocarriers generated in region B might immediately diffuse vertically to region A and go to the electrode. Therefore, the establishment of a more sophisticated model is required to deeply understand the carrier transport processes. To apply photoelectrical detection for highly sensitive magnetometry, it is crucial to efficiently collect the spin-dependent photocurrent from NV centers. However, a short diffusion length leads to a decrease in photocurrent in the low-electric field region. Since the increase in the photocurrent against the implantation dose is not linear, as shown in Fig. 4(a), there is a limit to the improvement in the photocurrent achieved by increasing the implantation dose. In addition, the graphitization of diamond under high-dose conditions is not trivial.<sup>23</sup> These facts suggest that a careful device design, such as dopant concentration and nitrogen ion dose, is required to improve the photocarrier generation due to the NV centers.

Continuous-wave PDMR (CW-PDMR) measurements were performed to demonstrate the electrical readout of the electron spin state of  $\text{NV}^-$  in the p-i-n diode. Figure 5(a) shows the PDMR spectra for the NV centers below the  $\text{p}^+$ -region at a laser power of 4 mW and a

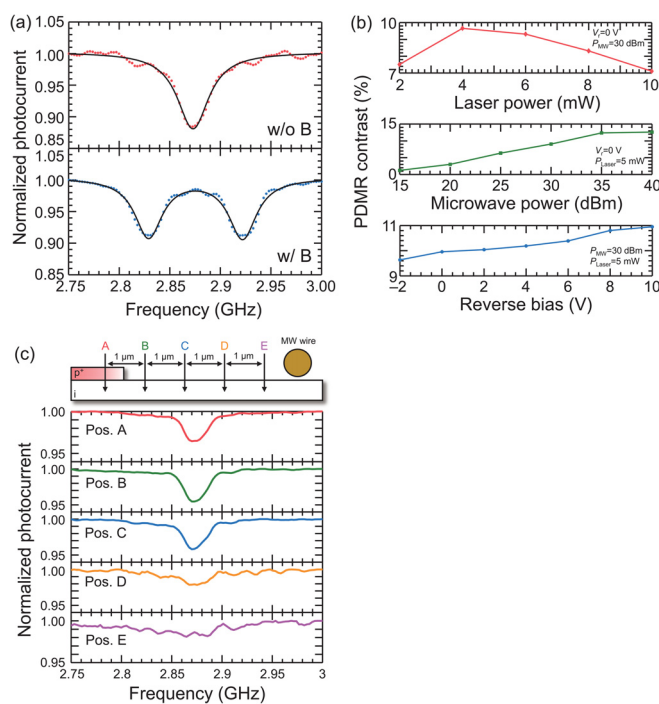


**FIG. 5.** PDMR observations. (a) PDMR spectra with and without a static magnetic field at 10 V, measured below the  $\text{p}^+$ -region. The solid curves are fits using Lorentzian curves. (b) PDMR contrast as a function of the laser power, microwave power, and applied voltage. (c) Position dependence of the PDMR spectrum measured in the photovoltaic mode (0 V). The spectra shown in panels (a) and (c) were obtained at a laser power of 4 mW and a microwave power of 30 dBm. Panels (a) and (b) were obtained by using sample #h879, and panel (c) was obtained by using sample #h877.

microwave power of 30 dBm for a total integration time of 80 s for each spectrum. The microwaves were irradiated through a  $20 \mu\text{m}$  Cu wire transversely placed against the direction of the p-i-n device. The PDMR spectrum showed a clear dip at approximately 2.87 GHz without a bias magnetic field, while the dip was found to split under a magnetic field owing to the Zeeman shift of the spin levels. Figure 5(b) shows the PDMR contrast as a function of the laser power, microwave power, and voltage applied to the device. The contrast was higher than 9% at laser powers of 4–6 mW and found to decrease at higher laser powers up to 10 mW. The PDMR contrast monotonically increased with the microwave power [middle in Fig. 5(b)], reaching a maximum value of 12.6% in the photovoltaic mode, while the linewidth continued to increase because of power broadening.<sup>24</sup> In the photovoltaic mode, the contrast had a maximum value of 12.6%, which is higher than previously reported CW-PDMR contrasts with single-beam excitation.<sup>5,12</sup> Notably, the simultaneously obtained optically detected magnetic resonance exhibited a contrast of  $\sim 23\%$ , higher than the PDMR contrast, probably because the photocurrent included photocarriers from defects other than the NV centers such as P1 centers.<sup>5</sup> By applying techniques such as the pulse sequence,<sup>6</sup> microwave-triggering technique,<sup>11</sup> and dual-beam excitation,<sup>12</sup> the PDMR contrast and linewidth can be further improved. Upon the application of the voltage, the PDMR contrast gradually increased for the investigated voltage range [bottom in Fig. 5(b)]. This slight increase might be related to the charge conversion of the NV centers and/or other defects, resulting in the change of the background in the depletion layer. However, further investigations are necessary to understand this behavior in detail. Finally, we performed PDMR measurements at different positions from the  $\text{p}^+$ -edge at 0 V. Figure 5(c) shows a lateral schematic of the measured positions with respect to the  $\text{p}^+$ -edge. We observed PDMR dips at positions A, B, and C. Position C is  $\sim 1.6 \mu\text{m}$  away from the  $\text{p}^+$ -edge and thus outside the depletion layer. In contrast, at more distant positions, D and E, a clear PDMR dip was not observed. The measured signals contain both the spin-dependent photocurrent and background current including electrical noises. The spin-dependent signal is considered to depend on the measurement position as seen in Fig. 4. Conversely, electrical noises do not depend on measurement position. Thus, the SNR is deteriorated at the distant positions, leading to the disappearance of the PDMR dip.

Here, we investigated the photoelectrical performance at reverse voltages up to 10 V. Application of higher voltages will be important to investigate the behavior of the PDMR contrast, which is possibly affected by various factors such as background current, Stark effect, and charge conversion.<sup>25</sup> Moreover, a further increase in the voltage would lead to carrier multiplication to significantly increase the signal level. Photocurrent multiplication of tens to thousands of times is expected according to the reported avalanche-mode operation in devices based on other wide-gap semiconductors,<sup>26,27</sup> which can enhance the detection rate by several orders of magnitude. Notably, the avalanche mode increases not only the photocurrent but also the background current; thus, it is necessary to investigate the multiplication factor to obtain the optimum SNR. In the p-i-n structures including the vertical configuration,<sup>28,29</sup> the NV centers would suffer from the effects mentioned above in a high electric-field under an avalanche mode operation. Using a reach-through structure,<sup>30</sup> the photocarrier multiplication region and the NV center formation region can be separated, which can be expected to suppress the aforementioned effects.

The use of the reach-through structure also makes it possible to reduce the multiplication voltage, which is more advantageous for sensor applications compared to a simple p-i-n structure.

For integrated magnetometer systems,<sup>31</sup> photoelectrical detection will be a useful tool. The integrated system is mainly developed for highly sensitive magnetometers using numerous NV centers in a high detection volume.<sup>32,33</sup> However, for the device fabricated in this study, the minority carrier diffusion length is limited to  $< 2 \mu\text{m}$ . Thus, for the case of using a large detection volume, it is necessary to design the dimensions of the sensor system while considering the control of the diffusion length and depletion layer width by an applied voltage. The extension of the minority carrier diffusion length by optimizing the NV formation and dopant conditions is an important topic for further studies. In addition, although we fabricated NV centers at a relatively deep position of 350 nm from the surface in this study, shallow NV centers are relevant for quantum sensing,<sup>11,12</sup> e.g., detection of nano-scale NMR<sup>34–36</sup> and atomically thin two-dimensional materials.<sup>37–40</sup> Therefore, it would be interesting to investigate the effect of surface recombination/trapping on the estimation of the minority carrier diffusion length for shallow NV centers.

In conclusion, the photoelectrical readout of NV<sup>-</sup> centers by utilizing lateral diamond p-i-n diodes was demonstrated. The laser power dependence of the photocurrent showed a quadratic increase based on the two-photon ionization process. We investigated the transport mechanism for minority carriers generated from NV centers. The diffusion length was found to decrease when the photocarriers passed through the defective implantation region, particularly at a high nitrogen ion dose. The PDMR signal was found to depend on the measurement position and disappeared at positions more than  $\sim 1.6 \mu\text{m}$  away from the p<sup>+</sup>-region, which is owing to the deterioration of the SNR. The PDMR spectra were measured under various conditions, and a maximum contrast of  $\sim 12\%$  was obtained. The photocurrent and PDMR spectra were measured even at 0 V using the built-in potential of the diamond device, while both the photocurrent and the PDMR contrast were found to gradually increase upon application of voltages up to 10 V. The utilization of an electronic device for the photoelectrical detection of NV centers will improve quantum sensors, particularly for the fabrication of an integrated quantum system.

See the [supplementary material](#) for the nitrogen distribution simulated by SRIM and the details of the electric field simulation with TCAD.

This study was supported by the MEXT Quantum Leap Flagship Program (MEXT Q-LEAP) Grant No. JPMXS0118067395 and MEXT/JSPS KAKENHI Grant No. 18H01472, Japan. The authors thank the technical staff at AIST, who helped in fabricating the device.

## DATA AVAILABILITY

The data that support the findings of this study are available from the corresponding author upon reasonable request.

## REFERENCES

- J. R. Maze, P. L. Stanwix, J. S. Hodges, S. Hong, J. M. Taylor, P. Cappellaro, L. Jiang, M. V. G. Dutt, E. Togan, A. S. Zibrov, A. Yacoby, R. L. Walsworth, and M. D. Lukin, *Nature* **455**, 644 (2008).
- G. Balasubramanian, I. Y. Chan, R. Kolesov, M. Al-Hmoud, J. Tisler, C. Shin, C. Kim, A. Wojcik, P. R. Hemmer, A. Krueger, T. Hanke, A. Leitenstorfer, R. Bratschkitsch, F. Jelezko, and J. Wrachtrup, *Nature* **455**, 648 (2008).
- N. Mizuochi, T. Makino, H. Kato, D. Takeuchi, M. Ogura, H. Okushi, M. Nothaft, P. Neumann, A. Gali, F. Jelezko, J. Wrachtrup, and S. Yamasaki, *Nat. Photonics* **6**, 299 (2012).
- H. R. Philipp and E. A. Taft, *Phys. Rev.* **127**, 159 (1962).
- E. Bourgeois, A. Jarmola, P. Siyushev, M. Gulka, J. Hruby, F. Jelezko, D. Budker, and M. Nesladek, *Nat. Commun.* **6**, 8577 (2015).
- F. M. Hrubesch, G. Braunbeck, M. Stutzmann, F. Reinhard, and M. S. Brandt, *Phys. Rev. Lett.* **118**, 037601 (2017).
- P. Siyushev, M. Nesladek, E. Bourgeois, M. Gulka, J. Hruby, T. Yamamoto, M. Trupke, T. Teraji, J. Isoya, and F. Jelezko, *Science* **363**, 728 (2019).
- H. Morishita, S. Kobayashi, M. Fujiwara, H. Kato, T. Makino, S. Yamasaki, and N. Mizuochi, *Sci. Rep.* **10**, 792 (2020).
- M. Gulka, D. Wirtitsch, V. Ivády, J. Vodnik, J. Hruby, G. Magchiels, E. Bourgeois, A. Gali, M. Trupke, and M. Nesladek, *arXiv:2101.04769* (2021).
- E. Bourgeois, M. Gulka, and M. Nesladek, *Adv. Opt. Mater.* **8**, 1902132 (2020).
- M. Gulka, E. Bourgeois, J. Hruby, P. Siyushev, G. Wachter, F. Aumayr, P. R. Hemmer, A. Gali, F. Jelezko, M. Trupke, and M. Nesladek, *Phys. Rev. Appl.* **7**, 044032 (2017).
- E. Bourgeois, E. Londero, K. Buczak, J. Hruby, M. Gulka, Y. Balasubramanian, G. Wachter, J. Stursa, K. Dobes, F. Aumayr, M. Trupke, A. Gali, and M. Nesladek, *Phys. Rev. B* **95**, 041402 (2017).
- Y. Doi, T. Fukui, H. Kato, T. Makino, S. Yamasaki, T. Tashima, H. Morishita, S. Miwa, F. Jelezko, Y. Suzuki, and N. Mizuochi, *Phys. Rev. B* **93**, 081203(R) (2016).
- M. Shimizu, T. Makino, T. Iwasaki, J. Hasegawa, K. Tahara, W. Naruki, H. Kato, S. Yamasaki, and M. Hatano, *Diamond Relat. Mater.* **63**, 192 (2016).
- S. G. Ri, D. Takeuchi, C. E. Nebel, N. Tokuda, Y. Yamazaki, S. Yamasaki, and H. Okushi, *Diamond Relat. Mater.* **16**, 831 (2007).
- J. F. Ziegler, M. D. Ziegler, and J. P. Biersack, *Nucl. Instrum. Methods Phys. Res., Sect. B* **268**, 1818 (2010).
- T. Lühmann, R. John, R. Wunderlich, J. Meijer, and S. Pezzagna, *Nat. Commun.* **10**, 4956 (2019).
- E. D. Herbschleb, H. Kato, Y. Maruyama, T. Danjo, T. Makino, S. Yamasaki, I. Ohki, K. Hayashi, H. Morishita, M. Fujiwara, and N. Mizuochi, *Nat. Commun.* **10**, 3766 (2019).
- H. Kato, M. Wolfer, C. Schreyvogel, M. Kunzer, W. Müller-Sebert, H. Obloh, S. Yamasaki, and C. Nebel, *Appl. Phys. Lett.* **102**, 151101 (2013).
- M. Shimizu, T. Makino, T. Iwasaki, K. Tahara, H. Kato, N. Mizuochi, S. Yamasaki, and M. Hatano, *Appl. Phys. Express* **11**, 033004 (2018).
- H. Hamad, D. Planson, C. Raynaud, and P. Bevilacqua, *Semicond. Sci. Technol.* **32**, 054001 (2017).
- H. Kato, T. Makino, M. Ogura, D. Takeuchi, and S. Yamasaki, *Diamond Relat. Mater.* **34**, 41 (2013).
- R. Kalish, A. Reznik, S. Prawer, D. Saada, and J. Adler, *Phys. Status Solidi A* **174**, 83 (1999).
- A. Dréau, M. Lesik, L. Rondin, P. Spinicelli, O. Arcizet, J.-F. Roch, and V. Jacques, *Phys. Rev. B* **84**, 195204 (2011).
- D. A. Broadway, N. Dentschuk, A. Tsai, S. E. Lillie, C. T. K. Lew, J. C. McCallum, B. C. Johnson, M. W. Doherty, A. Stacey, L. C. L. Hollenberg, and J. P. Tetienne, *Nat. Electron.* **1**, 502 (2018).
- S.-C. Shen, Y. Zhang, D. Yoo, J.-B. Limb, J.-H. Ryou, P. D. Yoder, and R. D. Dupuis, *IEEE Photonics Technol. Lett.* **19**, 1744 (2007).
- H. Liu, D. McIntosh, X. Bai, H. Pan, M. Liu, J. C. Campbell, and H. Y. Cha, *IEEE Photonics Technol. Lett.* **20**, 1551 (2008).
- T. Iwasaki, W. Naruki, K. Tahara, T. Makino, H. Kato, M. Ogura, D. Takeuchi, S. Yamasaki, and M. Hatano, *ACS Nano* **11**, 1238 (2017).
- B. Yang, T. Murooka, K. Mizuno, K. Kim, H. Kato, T. Makino, M. Ogura, S. Yamasaki, M. E. Schmidt, H. Mizuta, A. Yacoby, M. Hatano, and T. Iwasaki, *Phys. Rev. Appl.* **14**, 044049 (2020).
- R. J. McIntyre, P. P. Webb, and H. Dautet, *IEEE Trans. Nucl. Sci.* **43**, 1341 (1996).
- N. H. Wan, T. J. Lu, K. C. Chen, M. P. Walsh, M. E. Trusheim, L. De Santis, E. A. Bersin, I. B. Harris, S. L. Mouradian, I. R. Christen, E. S. Bielejec, and D. Englund, *Nature* **583**, 226 (2020).

- <sup>32</sup>T. Wolf, P. Neumann, K. Nakamura, H. Sumiya, T. Ohshima, J. Isoya, and J. Wrachtrup, *Phys. Rev. X* **5**, 041001 (2015).
- <sup>33</sup>J. F. Barry, M. J. Turner, J. M. Schloss, D. R. Glenn, Y. Song, M. D. Lukin, H. Park, and R. L. Walsworth, *Proc. Natl. Acad. Sci. U. S. A.* **113**, 14133 (2016).
- <sup>34</sup>N. Aslam, M. Pfender, P. Neumann, R. Reuter, A. Zappe, F. F. De Oliveira, A. Denisenko, H. Sumiya, S. Onoda, J. Isoya, and J. Wrachtrup, *Science* **357**, 67 (2017).
- <sup>35</sup>S. J. Devience, L. M. Pham, I. Lovchinsky, A. O. Sushkov, N. Bar-Gill, C. Belthangady, F. Casola, M. Corbett, H. Zhang, M. Lukin, H. Park, A. Yacoby, and R. L. Walsworth, *Nat. Nanotechnol.* **10**, 129 (2015).
- <sup>36</sup>H. Ishiwata, M. Nakajima, K. Tahara, H. Ozawa, T. Iwasaki, and M. Hatano, *Appl. Phys. Lett.* **111**, 043103 (2017).
- <sup>37</sup>I. Lovchinsky, J. D. Sanchez-Yamagishi, E. K. Urbach, S. Choi, S. Fang, T. I. Andersen, K. Watanabe, T. Taniguchi, A. Bylinskii, E. Kaxiras, P. Kim, H. Park, and M. D. Lukin, *Science* **355**, 503 (2017).
- <sup>38</sup>J.-P. Tetienne, N. Donschuk, D. A. Broadway, A. Stacey, D. A. Simpson, and L. C. L. Hollenberg, *Sci. Adv.* **3**, e1602429 (2017).
- <sup>39</sup>M. J. H. Ku, T. X. Zhou, Q. Li, Y. J. Shin, J. K. Shi, C. Burch, L. E. Anderson, A. T. Pierce, Y. Xie, A. Hamo, U. Vool, H. Zhang, F. Casola, T. Taniguchi, K. Watanabe, M. M. Fogler, P. Kim, A. Yacoby, and R. L. Walsworth, *Nature* **583**, 537 (2020).
- <sup>40</sup>L. Thiel, Z. Wang, M. A. Tschudin, D. Rohner, I. Gutiérrez-Lezama, N. Ubrig, M. Gibertini, E. Giannini, A. F. Morpurgo, and P. Maletinsky, *Science* **364**, 973 (2019).